Kinetics of trifurcated electron flow in the decaheme bacterial proteins MtrC and MtrF

Xiuyun Jiang[a], Bastian Burger[a,b], Fruzsina Gajdos[a], C. Bortolotti[c], Zdenek Futera[a], Marian Breuer[a], and Jochen Blumberger[a,d,1]

[a]Department of Physics and Astronomy, University College London, London WC1E 6BT, United Kingdom; [b]Department of Chemistry, Technische Universität München, D-85747 Garching, Germany; [c]Department of Life Sciences, Universita degli Studi di Modena e Reggio Emilia, 41121 Modena, Italy; and [d]Institute for Advanced Study, Technische Universität München, D-85748 Garching, Germany

Edited by Michael L. Klein, Institute of Computational Molecular Science, Temple University, Philadelphia, PA, and approved January 8, 2019 (received for review October 21, 2018)

The bacterium *Shewanella oneidensis* has evolved a sophisticated electron transfer (ET) machinery to export electrons from the cytosol to extracellular space during extracellular respiration. At the heart of this process are decaheme proteins of the Mtr pathway, MtrC and MtrF, located at the external face of the outer bacterial membrane. Crystal structures have revealed that these proteins bind 10 c-type hemes arranged in the peculiar shape of a staggered cross that trifurcates the electron flow, presumably to reduce extracellular substrates while directing electrons to neighboring multiheme cytochromes at either side along the membrane. Especially intriguing is the design of the heme junctions trifurcating the electron flow: they are made of coplanar and T-shaped heme pair motifs with relatively large and seemingly unfavorable tunneling distances. Here, we use electronic structure calculations and molecular simulations to show that the side chains of the heme rings, in particular the cysteine linkages inserting in the space between coplanar and T-shaped heme pairs, strongly enhance electronic coupling in these two motifs. This results in an $\approx 10^3$-fold speedup of ET steps at heme junctions that would otherwise be rate limiting. The predicted maximum electron flux through the solvated proteins is remarkably similar for all possible flow directions, suggesting that MtrC and MtrF shuttle electrons with similar efficiency and reversibly in directions parallel and orthogonal to the outer membrane. No major differences in the ET properties of MtrC and MtrF are found, implying that the different expression levels of the two proteins during extracellular respiration are not related to redox function.

electron transfer | extracellular respiration | heme | molecular dynamics | density functional theory

Multiheme cytochromes are expressed by the bacteria *Shewanella oneidensis* and *Geobacter sulfurreducens* to shuttle electrons from the inside of the cell across the periplasm and outer membrane to extracellular space in a process termed extracellular respiration (1). They are part of a fascinating electron export machinery that allows the bacterium to survive at reduced O_2 levels by transferring electrons, accumulated by metabolic activity, to electron acceptors outside the cell (e.g., transition metal oxide minerals Fe_2O_3 and MnO_2). The bacteria's ability to electronically wire the cytosol with extracellular space has attracted much interest in their use in the cleanup of water and soil containing radioactive isotopes (2), mediatorless microbial fuel cells (3, 4), and microbial electrosynthesis (refs. 5–7; reviewed in ref. 8). The exquisite electron transfer (ET) properties of their multiheme cytochromes have also sparked much interest in their use in bioelectronic junctions and devices (9–12). It was recently shown that two multiheme cytochromes from *S. oneidensis*, STC and MtrF, are up to 1,000-fold more conductive than other metalloproteins, such as azurin and single-heme cytochromes (12), which might open up a host of electronic applications at the biotic/abiotic interface.

Crystal structures of several multiheme cytochromes have been resolved in recent years (13–17); the structures of some of the most prominent multiheme cytochromes of *S. oneidensis* are shown in Fig. 1. Among the largest, the decaheme proteins MtrC (17) and MtrF (15) (Fig. 1 *A* and *B*) arrange 10 tightly packed bis-His coordinated c-type hemes in the peculiar shape of a staggered cross: a vertically aligned octaheme chain is intersected horizontally by a tetraheme chain. Located on the external surface of the outer membrane, MtrC (MtrF) is part of the MtrCAB (MtrFDE) complex that spans the outer membrane (Fig. 1*E*) and transmits electrons over distances larger than 100 Å. Electron input from the electron donor MtrA (MtrD) occurs at one of the termini of the octaheme chain, speculated to be heme 10 (15). Subsequent electron flow through MtrC (MtrF) may occur in three different directions: along the octaheme chain to heme 5 or toward the side exits of the tetraheme chain, hemes 2 and 7.

While there may be multiple reasons for the evolution of cytochromes that feature a staggered heme cross, a clue for a possible functional role came from recent in vivo (18) and electron cryotomography studies (19). It was shown that the micrometer-long cellular appendages that *S. oneidensis* form on reduced O_2 levels (sometimes referred to as "biological nanowires") are in fact extensions of the outer membrane rather than pilin-based structures (20, 21), with MtrCAB distributed

Significance

Certain bacteria survive in anoxic environments by switching from aerobic to anaerobic respiration: in place of O_2, they reduce diverse substrates outside the cell. Multiheme cytochromes spanning the outer membrane have been identified as the essential building blocks for this process. Here, we provide molecular-level insight into the electron flow in two decaheme proteins. Our study reveals that electron hopping through these proteins is strongly enhanced by cysteines at heme junctions that trifurcate the electron flow. We believe this to be a general design principle in multiheme cytochromes for acceleration of electron transfer (ET) steps that would otherwise be too slow for respiration. Our study uncovers a natural design principle of significance to an entire class of proteins involved in biological ET.

Author contributions: M.B. and J.B. designed research; X.J., B.B., F.G., and C.B. performed research; Z.F. contributed new reagents/analytic tools; X.J., B.B., F.G., C.B., M.B., and J.B. analyzed data; and J.B. wrote the paper.

The authors declare no conflict of interest.

This article is a PNAS Direct Submission.

[1]To whom correspondence should be addressed. Email: j.blumberger@ucl.ac.uk.

This article contains supporting information online at www.pnas.org/lookup/suppl/doi:10.1073/pnas.1818003116/-/DCSupplemental.

Published online February 12, 2019.

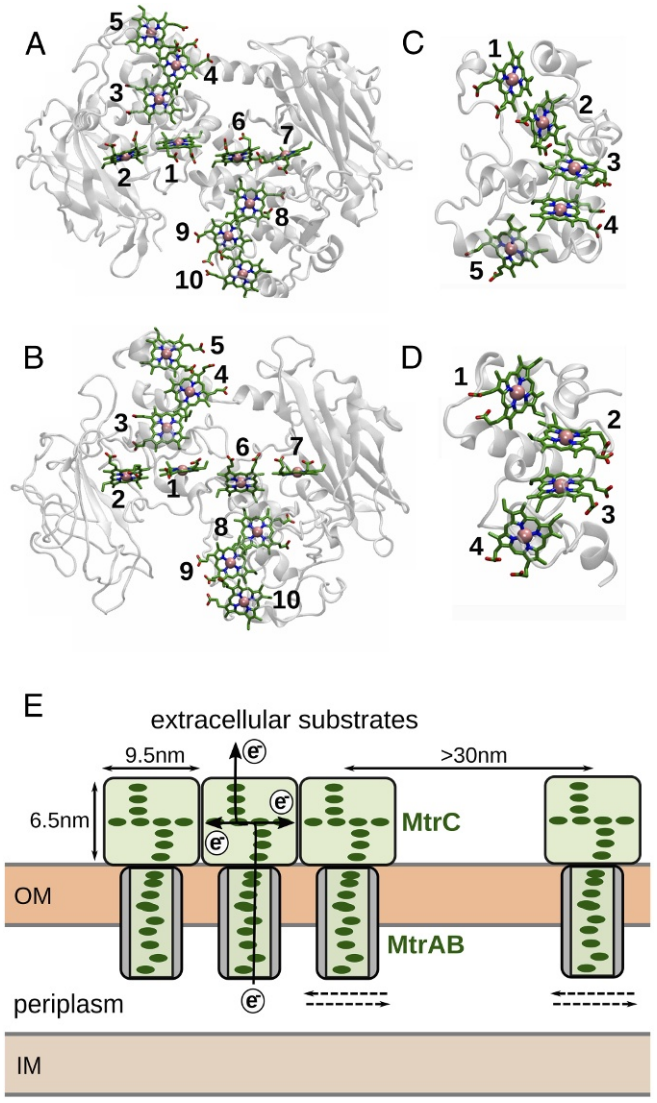

Fig. 1. Crystal structures of decaheme cytochromes MtrC (PDB ID code 4LM8; *A*) (17) and MtrF (PDB ID code 3PMQ; *B*) (15), pentaheme cytochrome NrfB (PDB ID code 2OZY; *C*) (13), and tetraheme cytochrome STC (PDB ID code 1M1Q; *D*) (48). The bis-His coordinated *c*-type heme rings are depicted in green, Fe atoms are in purple, and the protein secondary structures are in gray. (*E*) Cartoon representation of a possible arrangement of MtrCAB complexes in the bacterial outer membrane (OM) during extracellular respiration inspired by the cryotomography study in ref. 19. Electrons from the periplasm are transferred across the OM via the decaheme protein complex MtrAB and passed onto the decaheme protein MtrC, where the electron flow is trifurcated in directions parallel and orthogonal to the OM. The spacing between the centers of adjacent MtrC and MtrA molecules is typically about 10 nm (i.e., close contact), but gaps larger than 30 nm were also observed and may be overcome by lateral protein diffusion within the membrane as indicated by dashed arrows (19). IM, inner bacterial membrane.

along their length (18, 19) as schematically indicated in Fig. 1*E*. Adjacent MtrCAB complexes are thought to interact via the tetraheme chains of MtrC to facilitate micrometer-long electron transfer along the outer membrane as observed by conductive atomic force microscopy (c-AFM) (22), while the octaheme chains support ET away from the membrane and onto extracellular substrates. In this way, the heme cross motif helps supply the surface of the membrane with electrons while reducing extracellular substrates. However, the kinetics of the trifurcated electron flow in MtrC remains to be elucidated. Does this protein transfer electrons equally well in the direction parallel to the membrane and away from it?

In our previous work, we used quantum chemistry and molecular simulation to obtain insight into the workings of solvated multiheme cytochromes at the single-protein level (23–25). In an early study, we calculated the reduction potentials for all 10 hemes in all-oxidized (all-ox) MtrF using molecular dynamics (MD) simulation (26), and more recently, Barrozo et al. (27) reported heme reduction potentials for MtrF and MtrC in the all-ox and all-reduced states. Both studies agreed that the free energy profile for electron flow along the protein has ups and downs, resulting in near-thermoneutral ET along the octaheme chain. In terms of kinetics, we found that heme–heme electronic couplings are about three orders of magnitude smaller than reorganization free energy, which implies that intraprotein ET through solvated multiheme cytochromes occurs via heme-to-heme hopping. However, our calculations fell short of reproducing the approximately nanoampere currents reported in scanning tunneling microscopy (STM) measurements (9, 11). Even after accounting for partial protein hydration in these experiments, the computed STM currents remained underestimated by about two orders of magnitude.

This discrepancy has motivated us to take a closer look at the staggered cross heme motif built into MtrC and MtrF. The trifurcation of the electron flow is established by two junctions in the middle of the protein composed of T-shaped (8–6, 1–3) and coplanar heme pairs (6–1, 6–7, 1–2). Inspection of the crystal structure reveals relatively large heme-to-heme edge distances in these motifs, suggesting that the ET steps across the junctions may limit to overall electron flow through the protein. In this respect, we note that the smaller tetraheme protein STC (Fig. 1*D*) also features two T-shaped heme pairs, such as in MtrF and MtrC, although no coplanar pairs. We found that cysteine linkages, which chemically attach the heme rings to the protein frame, enhance electronic coupling between the T-shaped heme pairs in STC. The effect of the cysteine linkages has not been included in our previous computations on MtrF (28) and calls for a recalculation of electronic couplings for this protein, especially in the context of the persisting mismatch between computation and experiment for STM currents (11).

Returning to the bacterium *S. oneidensis*, a puzzling observation is that, under anoxic conditions, only MtrCAB is expressed and that MtrDEF is not expressed, although it is known that MtrF can functionally replace MtrC (29, 30). As pointed out by Barrozo et al. (27), this apparent redundancy is unusual, and the conditions under which the genes for MtrDEF are expressed remain largely unknown. It begs the question of whether different expression levels of the two proteins are due to differences in their ET properties. Does MtrC conduct electrons better than MtrF? To answer this and the above questions, we present in this paper all ET parameters, heme-to-heme ET rate constants, and protein-limited electron flux through MtrC calculated for exactly the same conditions as for MtrF. This undertaking is very timely, because the crystal structure of MtrC has recently become available. While Barrozo et al. (27) have recently presented a preliminary characterization of the ET kinetics for MtrC, although with outdated electronic couplings from MtrF, a full and up-to-date characterization for this protein is outstanding.

Results

Heme–Heme Electronic Interaction. Electronic coupling matrix elements for electron hopping between adjacent $Fe^{2+}Fe^{3+}$-heme pairs have been calculated along MD trajectories for the solvated MtrC and MtrF. The coupling calculations were carried out for two quantum mechanical (QM) models on structures extracted from the MD run: one where the two bis-His hemes are modeled by unsubstituted Fe-porphin rings axially ligated by

two N-methyl imidazoles, hereafter referred to as the minimum model, and one where, in addition, all of the side chains of both heme rings are included, hereafter referred to as the large model. Details on the MD simulations and the density functional theory (DFT)-based coupling calculations can be found in *Materials and Methods* and *SI Appendix*.

The results are shown in Fig. 2, where we have also included previously reported couplings for the small tetraheme protein STC (31). The data for the minimum model (Fig. 2*A*) show the expected exponential decay with respect to the heme edge-to-heme edge distance r, $\langle|H_{ab}|^2\rangle^{1/2} = A\exp[-\beta(r-r_0)/2]$. The scatter around the mean values is due to thermal motion of the heme rings ($T = 300$ K). The couplings decrease in the order stacked > T-shaped > coplanar heme–heme motif. In the stacked motif, the hemes approach one another up to van der Waals distance (3.5–5 Å), resulting in couplings of several millielectronvolts (meV), whereas in the T-shaped and coplanar motifs, the edge-to-edge distances are larger (5–8 Å), and the couplings are an order of magnitude smaller, typically a few 0.1 meV or less. The distance decay constant β and the prefactor A are determined to be 2.26 Å^{-1} and 3.49 meV, respectively ($R^2 = 0.99$, $r_0 = 3.6$ Å), in good agreement with the ones reported previously for data from MtrF only (28). The thermally averaged couplings for each heme pair of MtrC are depicted in Fig. 2*B*, clearly illustrating how the couplings decrease from relatively large values for the stacked motif at electron input and exit sites of the octaheme chain (hemes 10 and 5) to smaller values for the T-shaped and coplanar motifs in the middle of the protein. Particularly small is the electronic coupling for the coplanar pair 1-6 in the center of the protein due to the relatively large edge-to-edge distance [7.0 Å in the crystal structure (17)].

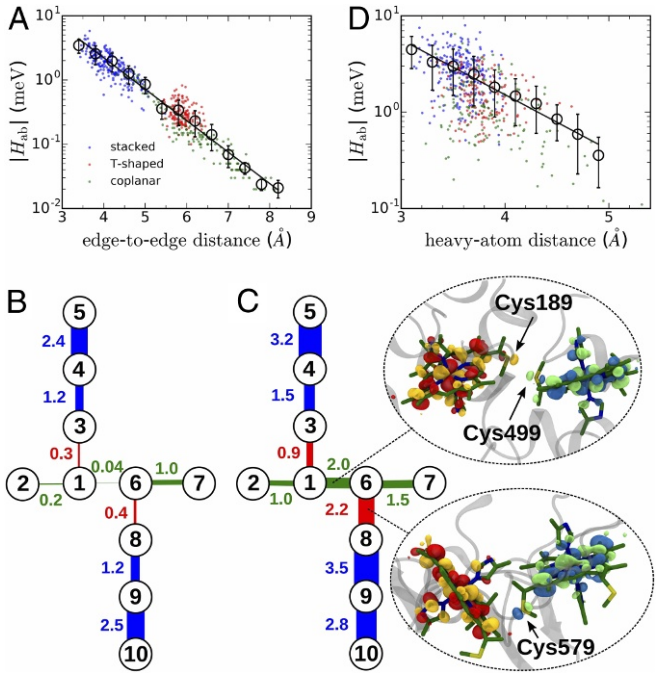

Fig. 2. Heme–heme electronic coupling matrix elements, $|H_{ab}|$, in MtrC, MtrF, and STC. The distance dependence of electronic couplings is shown in *A* for the minimum QM model ($H_{ab} = H_{ab}^{m}$) composed of the unsubstituted heme rings plus axial ligands and in *D* for the large QM model ($H_{ab} = H_{ab}^{l}$), where, in addition, all heme side chains are included, in particular the Cys linkages. The couplings are calculated on structures obtained from MD simulation at room temperature. They are color coded according to the relative orientations of electron donating and accepting hemes: stacked motif in blue (heme pairs 10–9, 9–8, 3–4, and 4–5 in MtrC and MtrF and 2–3 in STC), T shaped in red (8–6 and 1–3 in MtrC and MtrF and 1–2 and 3–4 in STC), and coplanar in green (6–1, 6–7, and 1–2 in MtrC and MtrF). Root-mean-square averages of the scattered data points were calculated for bins of width 0.4 (*A*) and 0.2 Å (*D*) and are denoted by black circles, with error bars indicating the root-mean-square fluctuations. Fits to an exponential are indicated by black lines. In *A*, the shortest heme edge-to-edge distance is used, and in *D*, the shortest distance between any heavy atom of heme ring and side chains is used. Electronic couplings averaged for each adjacent heme pair in MtrC, $\langle|H_{ab}|^2\rangle^{1/2}$, are indicated for the minimum QM model (*B*) and for the large QM model (*C*). The thickness of the bars connecting adjacent hemes is proportional to the average coupling. *C*, *Insets* depict the enhancement of electronic couplings due to Cys linkages inserting in the space between coplanar heme pair 6–1 and T-shaped heme pair 8–6. One of the three Fe $d(t_{2g})$-heme orbitals on electron donor and acceptor hemes contributing to electronic coupling are drawn as red/yellow and green/blue isosurfaces (denoted d_i^D and d_j^A in *SI Appendix*). Similar coupling enhancements are found for MtrF.

However, the situation is strikingly different when the heme side chains are included in the coupling calculation. While the values for the stacked motif hardly change, they increase significantly for coplanar and T-shaped motifs to values that are just slightly below the ones for the stacked motif (Fig. 2*C*). Consequently, all couplings now fall in a rather narrow range of about 0.9 to 3.5 meV for MtrC (from 0.7 to 4.5 meV for MtrF). For additional discussion, we define the coupling enhancement as the ratio $r_{dft}^{1/2} = [\langle|H_{ab}^{l}|^2\rangle/\langle|H_{ab}^{m}|^2\rangle]^{1/2}$, where H_{ab}^{l} and H_{ab}^{m} are the coupling matrix elements for heme-to-heme electron tunneling for the large (l) and minimum (m) QM models and $\langle\cdots\rangle$ denotes the thermal average over MD snapshots. We find that most of the coupling enhancement is due to the cysteine linkages that insert in the space between coplanar and T-shaped heme motifs (Fig. 2*C*, *Inset*). In the case of the coplanar heme pair 1-6, where the coupling enhancement effect is the greatest [$r_{dft}^{1/2} = 50$ for MtrC (30 for MtrF)], Cys189(197) and Cys499(476), which covalently link hemes 1 and 6 to the protein backbone, approach one another up to an S–S distance of 4.0 (3.8) Å. According to our calculations, the sulfur 3p orbital of Cys189(197) weakly mixes with the Fe-heme frontier orbitals of heme 1, and a similar mixing occurs for Cys499(476) and heme 6. The small delocalization of the frontier orbital over the S atoms leads to a sizable increase in orbital overlap and consequently, electronic coupling. Similar, albeit smaller, coupling enhancements occur for the T-shaped pairs 8–6 [$r_{dft}^{1/2} = 6$ (8)] and 1–3 [$r_{dft}^{1/2} = 3$ (4)], where only one cysteine inserts between the hemes.

A consequence of the mixing of frontier orbital amplitude over heme side chains is that the heme edge-to-heme edge distance is no longer a good distance metric for heme-to-heme electron tunneling. The spread of coupling values around the best fit for exponential distance decay is very large ($R^2 = 0.57$) (*SI Appendix*, Fig. S1). Instead, we use the shortest distance between any heavy atom (C, N, O, S) of the porphin ring plus side chains. Using this metric, all couplings shift to shorter distances and can be fit to an exponential distance decay with parameters similar to the ones for the minimum model in Fig. 2*A*, $\beta = 2.63$ Å^{-1}, $A = 2.57$ meV ($R^2 = 0.97$) (Fig. 2*D*), characteristic of through-space tunneling. However, the scatter around the mean values is still significantly larger than for the minimum model. Most likely, this is because the degree of delocalization of the frontier orbitals over the side chains varies more strongly with intramolecular heme geometry than for the unsubstituted porphyrine rings, and this effect is independent on interheme distance.

We would like to emphasize that electronic couplings calculated here are for through-space tunneling between adjacent heme cofactors including all side chains and the Cys linkages of the heme groups. Hence, the β values reported here are about a factor of two larger than the typical range for

through-protein tunneling, 1.0–1.5 $Å^{-1}$ (25), while the tunneling distance for each consecutive hop is about a factor of two or more smaller than for typical through-protein tunneling processes. As is well known, over distances of several nanometers and beyond, multistep hopping outcompetes one-step tunneling due to its favorable $1/R$ scaling compared with exponential scaling for one-step tunneling (25). There are amino acid side chains that bridge the gap between coplanar and T-shaped heme pairs (e.g., between hemes 1 and 6, ILE252, LEU571 in MtrC and PRO540, PRO243 in MtrF), implying that amino acid-mediated heme-to-heme tunneling could be an alternative mechanism. However, using pathway calculations (32, 33), we found that the dominant through-space tunneling path always gave couplings at least an order of magnitude higher than any amino acid-mediated pathway, which rules out this alternative mechanism, at least at the level of pathway calculations.

Reorganization Free Energy and Driving Force. We have calculated the reorganization free energy λ for ET between all adjacent hemes in MtrC using MD simulations. For the purpose of deriving fit parameters for λ in multiheme cytochromes, we also computed λ for the pentaheme cytochrome NrfB and take values for MtrF (34) and STC (31) from our previous work. We find that the values for all four proteins fall in the range 0.7–1.1 eV, with values for MtrC being slightly smaller on average than for MtrF (*SI Appendix*, Table S1). Interestingly, the dominating outer-sphere reorganization free energy due to protein and solvent, λ_o, does not correlate with the solvent-accessible surface area (SA) of the heme pairs (Fig. 3*A*) but can be well described by Marcus continuum formula if the static dielectric constant is assumed to be a linear function of the SA, $\epsilon_s(SA) = a + bSA$, a, b constants. The smallest mean deviation with respect to λ_o from MD is obtained for $a = 5.18$, $b = 0.016$ $Å^{-2}$, and an effective heme radius $r = 4.6$ Å [using an optical dielectric constant $\epsilon_{op} = 1.84$ (35)] (Fig. 3*B*). This gives ϵ_s values between 6 (for the buried heme pair 1–3 of MtrC) and 14 (for the strongly solvent exposed heme pair 10–9 of MtrF).

ET driving forces are calculated for the all-ox redox state of MtrC using MD combined with thermodynamic integration. The resultant free energy profile for ET along the heme chains (*SI Appendix*, Table S1) is qualitatively similar to the one reported recently by Barrozo et al. (27) for the same redox state, denoted the "electron hopping regime" in their work, and it is not further discussed here. For MtrF, ET driving forces are taken from our previous work (26).

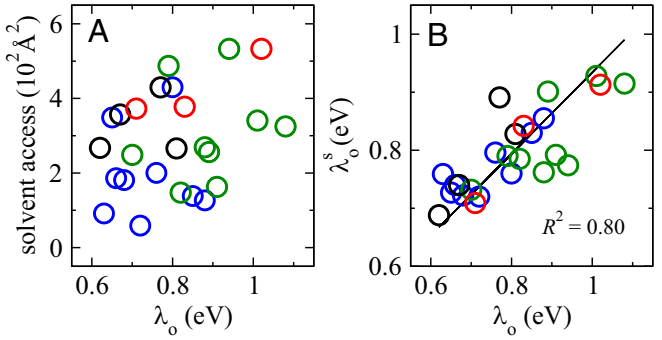

Fig. 3. Outer-sphere reorganization free energy, λ_o, for heme-to-heme ET in MtrC (blue), MtrF (green), NrfB (black), and STC (red) as obtained from MD simulations. Values for MtrC and NrfB are taken from present simulations (*SI Appendix*, Table S1), values for MtrF are taken from ref. 34, and values for STC are taken from ref. 31. Correlations are shown between λ_o and (*A*) the solvent-accessible SA (49) of corresponding heme pairs or (*B*) Marcus continuum estimates for outer-sphere reorganization free energy, λ_o^s, with SA-dependent static dielectric constant (details are in the text).

Electron Flux Through MtrC and MtrF. The computed electronic couplings, reorganization free energies, and driving forces are used to calculate the nonadiabatic (Marcus) rate constants for all heme-to-heme ET steps. They are used as an input for a chemical Master equation for electron hopping, which we solve to obtain the maximum protein-limited electron flux through MtrC and MtrF. Briefly, we assume fast and irreversible electron input in a given terminal heme site (e.g., heme 10) and electron output from another terminal heme site (e.g., heme 5). The electron population of each single heme, which can take values between zero (fully oxidized) and one (fully reduced), is determined subject to the condition of steady-state electron flux through the protein. Similar flux calculations are carried out for the reverse direction along the octaheme chain and for ET from heme 10 and heme 5 to the side exits heme 7 and heme 2, respectively. Additional details on the calculations can be found in *SI Appendix*.

The results are illustrated in Fig. 4 for MtrC (Fig. 4*A*) and MtrF (Fig. 4*B*). The heme-to-heme rate constants are proportional to the width of the arrows connecting hemes, and the protein-limited electron flux for all 12 possible flow directions across MtrC and MtrF is shown in Fig. 4, *Insets* (in powers of 10 s^{-1}). The rate constants along the octaheme chains of MtrC and MtrF span four orders of magnitude from $\sim 10^5$ to 10^9 s^{-1}, and the electron flux is $\approx 10^5$ s^{-1} in both the $10 \rightarrow 5$ and $10 \leftarrow 5$ directions. Electron flow from heme 10 or 5 to the side exits 7 and 2 is similarly fast as along the octaheme main chain, about 10^5 s^{-1}, except for $10 \rightarrow 7$ due to the relatively high reduction potential of heme 7. However, the latter is subject to uncertainty as discussed previously (26, 27) and may be overestimated. The reverse flow from the side exit 7 or 2 to 10 and 5 is somewhat slower, typically about 10^4 s^{-1}, due to successive uphill steps involving coplanar and T-shaped motifs. Similar results are obtained when the sets of reduction potentials from Barrozo et al. (27) are used, with deviations of typically less than an order of magnitude (*SI Appendix*, Table S2). Overall, our results indicate that MtrC and MtrF conduct electrons about equally well along their main axis and in perpendicular directions with little or no directional bias.

While the electron flux (with all heme side chains included) is remarkably similar for all directions, the electron flux enhancement due to the side chains is not the same in every direction—on the contrary, depending on the number of coplanar and T-shaped heme pairs and their free energies for a given flow direction, the flux enhancement varies from a factor of 2 ($10 \rightarrow 7$ in MtrF, one T-shaped pair) to a factor of $\approx 10^3$ ($10 \rightarrow 5$ in MtrC, one coplanar and two T-shaped pairs). Without the Cys-mediated coupling enhancement, the coplanar or T-shaped heme pairs in the middle of the protein limit the electron flux, whereas with coupling enhancement, these ET steps become similarly fast as ET between stacked heme pairs. In this case, there is no longer a clearly flux-limiting ET step; the two slowest steps are within an order of magnitude.

Discussion

Although direct experimental estimates for heme-to-heme ET rate constants in solvated single-molecule MtrC and MtrF have not (yet) been reported, measurements have been carried out on related systems that lend support to some of our results. First, Butt and coworkers (36) investigated the MtrC-containing MtrCAB protein complex inserted in a proteoliposome and adsorbed on an Fe(III)-oxide nanoparticle. The electron flux from an excess soluble electron donor across the entire MtrCAB complex onto the oxide was determined to be 10^4 s^{-1}. It was shown that the rate was limited by the heterogeneous ET step

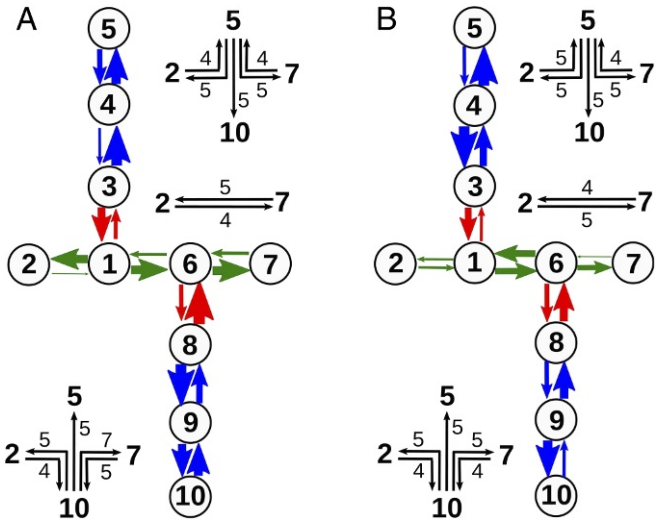

Fig. 4. Kinetics of trifurcated electron flow in solvated MtrC (*A*) and MtrF (*B*). The thickness of the colored arrows connecting hemes is proportional to the heme-to-heme ET rate constants in the all-ox state, which are summarized in *SI Appendix*, Table S1. Fig. 1 shows heme numbering. *Insets* show the possible flow directions between the terminal hemes 10, 5, 7, and 2, with the logarithm of the maximum protein-limited, steady-state electron flux, $\log_{10}(J_{max}/s^{-1})$, indicated for each flow direction. The electron flux is obtained by solving a chemical Master equation; details are in *Materials and Methods* and *SI Appendix*. J_{max} is taken from *SI Appendix*, Table S2 ("ox-sc").

from the protein to the oxide; hence, it should be considered a lower bound to the protein-limited rate. Our estimate for the latter, $10^5\ s^{-1}$, is thus in line with this experimental result.

Second, El-Naggar and coworkers (37) recently reported electrochemical gating experiments on *S. oneidensis* MR1 cells, which require the Mtr pathway cytochromes (in particular, MtrC) for ET to the electrodes. Measuring the conduction current as a function of temperature, Arrhenius behavior was observed, and the thermal activation energy for electron transport was determined to be 0.29 eV. This compares very favorably with the calculated largest activation free energy for heme-to-heme hopping steps along the octaheme chain, $\Delta A^{\ddagger} = (\lambda + \Delta A)^2/(4\lambda) = 0.33$ eV in the $10 \rightarrow 5$ direction (heme pair 6–1) and $\Delta A^{\ddagger} = 0.29$ eV in the $10 \leftarrow 5$ direction (heme pair 8–6).

Third, another type of experiment that one could compare our results with are the I-V measurements on single MtrC(9) and MtrF(11) proteins using STM. Assuming the same hopping mechanism as for ET in solution (11, 28, 38, 39), we obtain currents of a few 0.1 nA at 0.5-V bias voltage for MtrC and MtrF, in good agreement with experiments (9, 11) (*SI Appendix*, Fig. S2). By contrast, without the Cys-mediated electronic coupling enhancement, the currents are two orders of magnitude too low. The favorable comparison with the STM currents should be considered with some caution, however, since a number of assumptions went into the modeling (*SI Appendix* has the discussion). In this regard, we note that recent I-V measurements on MtrF monolayer junctions reported temperature-independent transport, which is incompatible with thermally activated hopping (12). However, the experimental conditions in this latter study are quite different with respect to the above-mentioned STM measurements (high vacuum vs. air, protein monolayer vs. single molecule, suspended nanowire vs. tip), which may tip the balance between different mechanisms.

Finally, we wish to investigate whether the popular pathway model (32, 33) can capture the rate enhancements due to the heme side chains as predicted by present DFT/projection operator-based diabatization (POD) calculations. To this end, we have calculated the enhancement factor $r_{pw} = \langle |H_{ab}^{pw}|^2 \rangle / \langle |H_{ab}^{ts}|^2 \rangle$, where H_{ab}^{pw} and H_{ab}^{ts} are the pathway coupling matrix elements for heme-to-heme electron tunneling along the strongest coupling path in the large QM model (typically through space via side chains) and in the minimum QM model (through space edge to edge) and $\langle \cdots \rangle$ denotes the thermal average over MD snapshots. In the following, we compare r_{pw} with r_{dft} as defined in *Results*. We find values $r_{pw} = 2200$ ($r_{dft} = 2{,}500$) for the coplanar heme pair 1–6 and 120 (36) and 170 (11) for the T-shaped heme pairs 8–6 and 1–3, respectively, for pathway (DFT/POD) calculations on MtrC, and we find similar results for MtrF (*SI Appendix*, Table S3). The agreement between pathway model and DFT/POD is excellent for the heme pair 1–6 that limits the overall electron flow. However, the pathway model incorrectly predicts rate enhancements of the same size if the S atom of the Cys linkage is changed into CH_2 (31). This problem could be addressed by including chemical specificity in a refined version of the pathway model.

Concluding Remarks

We found that both MtrC and MtrF form a trifurcated electron conduit that channels electrons with similar efficiency in perpendicular ($10 \leftrightarrow 5$) and parallel ($7 \leftrightarrow 2$) directions relative to the outer membrane. The electron flow is reversible, implying that both proteins not only support electron export but also, support electron import, a feature that enables electrode-driven electrosynthesis of chemicals inside the bacterial cell (5–8, 40). The trifurcation of the electron flow in MtrC and MtrF is achieved by two junctions in the middle of the protein composed of heme pairs with relatively large edge-to-edge tunneling distances (T shaped, coplanar). Intriguingly, our calculations indicate that the junctions do not slow down the electron flux, because Cys linkages inserting in the space between these heme pairs significantly enhance electronic coupling by reducing the effective tunneling distance. The same effect has been observed before for the two T-shaped pairs in the smaller tetraheme cytochrome STC (31), implying that the coupling enhancement could be an evolutionary design principle of significance to the entire class of multiheme cytochromes.

We note that there is little difference in the protein-limited electron flow through MtrC and MtrF. While reorganization free energies are slightly lower in MtrC than in MtrF, in line with reduced solvent-accessible SA of its hemes, no significant differences in electronic coupling are discernible. Thus, from the perspective of redox function, our characterization suggests that MtrC can be replaced by MtrF, which is, in fact, observed experimentally (29, 30). The higher expression levels of MtrCAB relative to MtrFDE at low O_2 concentrations (41) are thus more likely related to a genetic origin rather than ET function.

Efficient ET in MtrC in the direction parallel to the outer membrane is one of the prerequisites for micrometer-long electronic conduction along cellular appendages as observed in ref. 22. Whether ET within MtrCAB or between adjacent MtrCAB complexes is the flux-limiting process remains to be investigated. According to the cryomicroscopy study of ref. 19, adjacent MtrCAB complexes may be separated by more than 30 nm as depicted in Fig. 1*E*. Hence, the answer to this question will depend on the diffusivity of the MtrCAB protein complex in the outer membrane and the kinetics of the interprotein ET step between two interacting MtrC proteins. Modeling of these processes will require a crystal structure of MtrCAB and a suitable representation, possibly coarse grained to study its diffusivity on long timescales, as well as an atomistic structure of the MtrC–MtrC interface.

Materials and Methods

MD simulations were carried for aqueous MtrC and NrfB at room temperature starting from the crystal structures Protein Data Bank (PDB) ID codes 1M1Q (42) and 2OZY (13), respectively, using the AMBER03 force field (43) and the TIP3P water model (44). Driving forces (ΔA_{ji}) for MtrC and reorganization free energies (λ) for MtrC and NrfB were obtained from MD stimulation as described for MtrF (26, 34). Heme–heme electronic coupling matrix elements (H_{ab}) were calculated for MtrC and MtrF as described in ref. 31 using the POD method (45, 46) in combination with a modified Perdew–Burke–Ernzerhof (PBE) functional, where 50% generalized gradient approximation (GGA) exchange is replaced by Hartree–Fock exchange. This method showed excellent performance (46) against high-level ab initio reference values on dimers of the HAB11 database (47). Full computational details can be found in *SI Appendix*.

ACKNOWLEDGMENTS. We acknowledge the use of the University College London (UCL) Legion High Performance Facility (Legion@UCL). X.J. was supported by a PhD studentship cosponsored by the Chinese Scholarship Council and the University College London. Z.F. was supported by Engineering and Physical Sciences Research Council (EPSRC) Grant EP/M001946/1. J.B. was supported by the European Research Council under European Union Horizon 2020 Research and Innovation Program Grant 682539/SOFTCHARGE. Via our membership with the United Kingdom's Higher Education Commission (HEC) Materials Chemistry Consortium, which is funded by EPSRC Grant EP/L000202, this work used the ARCHER UK National Supercomputing Service (www.archer.ac.uk).

1. Myers CR, Nealson KH (1988) Bacterial manganese reduction and growth with manganese oxide as the sole electron acceptor. *Science* 240:1319–1321.
2. Zhuang K, Ma E, Lovley DR, Mahadevan R (2012) The design of long-term effective uranium bioremediation strategy using a community metabolic model. *Biotechnol Bioeng* 109:2475–2483.
3. Yi H, et al. (2009) Selection of a variant of geobacter sulfurreducens with enhanced capacity for current production in microbial fuel cells. *Biosens Bioelect* 24:3498–3503.
4. Fitzgerald LA, et al. (2012) Aggrandizing power output from shewanella oneidensis mr-1 microbial fuel cells using calcium chloride. *Biosens Bioelect* 31:492–498.
5. Ross DE, Flynn JM, Baron DB, Gralnick JA, Bond DR (2011) Towards electrosynthesis in shewanella: Energetics of reversing the mtr pathway for reductive metabolism. *PLoS One* 6:e16649.
6. Lovley DR (2012) Electromicrobiology. *Annu Rev Microbiol* 66:391–409.
7. Schroder U, Harnisch F, Angenent LT (2015) Microbial electrochemistry and technology: Terminology and classification. *Energy Environ Sci* 8:513–519.
8. Chong GW, Karbelkar AA, El-Naggar MY (2018) Nature's conductors: What can microbial multi-heme cytochromes teach us about electron transport and biological energy conversion? *Curr Opin Chem Biol* 47:7–17.
9. Wigginton NS, Rosso KM, Lower BH, Shi L, Hochella MFJ (2007) Electron tunneling properties of outer-membrane decaheme cytochromes from shewanella oneidensis. *Geochim Cosmochim Acta* 71:543–555.
10. Leung KM, et al. (2013) Shewanella oneidensis mr-1 bacterial nanowires exhibit p-type, tunable electronic behavior. *ACS Nano* 13:2407–2411.
11. Byun HS, Pirbadian S, Nakano A, Shi L, El-Naggar MY (2014) Kinetic Monte Carlo simulations and molecular conductance measurements of the bacterial decaheme cytochrome mtrf. *ChemElectroChem* 1:1932–1939.
12. Garg K, et al. (2018) Direct evidence for heme-assisted solid-state electronic conduction in multi-heme c-type cytochromes. *Chem Sci* 9:7304–7310.
13. Clarke TA, Cole JA, Richardson DJ, Hemmings AM (2007) The crystal structure of the pentahaem c-type cytochrome nrfb and characterization of its solution-state interaction with the penthaem nitrite reductase nrfa. *Biochem J* 406:19–30.
14. Paixao VB, et al. (2008) The solution structure of a tetraheme cytochrome from shewanella frigidimarina reveals a novel family structural motif. *Biochemistry* 47:11973–11980.
15. Clarke TA, et al. (2011) Structure of a bacterial cell surface decaheme electron conduit. *Proc Natl Acad Sci USA* 108:9384–9389.
16. Edwards MJ, et al. (2012) The crystal structure of the extracellular 11-heme cytochrome unda reveals a conserved 10-heme motif and defined binding site for soluble iron chelates. *Structure* 20:1275–1284.
17. Edwards MJ, et al. (2015) Redox linked flavin sites in extracellular decaheme proteins involved in microbe-mineral electron transfer. *Sci Rep* 5:11677.
18. Pirbadian S, et al. (2014) Shewanella oneidensis mr-1 nanowires are outer membrane and periplasmic extensions of the extracellular electron transport components. *Proc Natl Acad Sci USA* 111:12883–12888.
19. Subramanian P, Pirbadian S, El-Naggar MY, Jensen GJ (2018) Ultrastructure of shewanella oneidensis mr-1 nanowires revealed by electron cryotomography. *Proc Nat Acad Sci USA* 115:E3246–E3255.
20. Vargas M, et al. (2013) Aromatic amino acids required for pili conductivity and long-range extracellular electron transport in geobacter sulfurreducens. *mBio* 4:e00210–13.
21. Adhikari RY, Malvankar NS, Tuominen MT, Lovley DR (2016) Conductivity of individual geobacter pili. *RSC Adv* 6:8354–8357.
22. El-Naggar MY, et al. (2010) Electrical transport along bacterial nanowires from shewanella oneidensis mr-1. *Proc Natl Acad Sci USA* 107:18127–18131.
23. Blumberger J (2018) Electron transfer and transport through multi-heme proteins: Recent progress and future directions. *Curr Opin Chem Biol* 47:24–31.
24. Breuer M, Rosso KM, Blumberger J, Butt JN (2015) Multi-heme cytochromes in shewanella oneidensis mr-1: Structures, functions and opportunities. *J R Soc Interface* 12:20141117.
25. Blumberger J (2015) Recent advances in the theory and molecular simulation of biological electron transfer reactions. *Chem Rev* 115:11191–11238.
26. Breuer M, Zarzycki P, Blumberger J, Rosso KM (2012) Thermodynamics of electron flow in the bacterial deca-heme cytochrome mtrf. *J Am Chem Soc* 134: 9868–9871.
27. Barrozo A, El-Naggar MY, Krylov AI (2018) Distinct electron conductance regimes in bacterial decaheme cytochromes. *Angew Chem Int Ed Engl* 57:6805–6809.
28. Breuer M, Rosso KM, Blumberger J (2014) Electron flow in multi-heme bacterial cytochromes is a balancing act between heme electronic interaction and redox potentials. *Proc Nat Acad Sci USA* 111:611–616.
29. Bucking C, Popp F, Kerzenmacher S, Gescher J (2010) Involvement and specificity of shewanella oneidensis outer membrane cytochromes in the reduction of soluble and solid-phase terminal electron acceptors. *FEMS Microbiol Lett* 306:144–151.
30. Coursolle D, Gralnick JA (2012) Reconstruction of extracellular respiratory pathways for iron(iii) reduction in shewanella oneidensis strain mr-1. *Front Microbiol* 3:56.
31. Jiang X, et al. (2017) Cysteine linkages accelerate electron flow through tetra-heme protein stc. *J Am Chem Soc* 139:17237–17240.
32. Beratan DN, Onuchic JN, Hopfield JJ (1987) Electron tunneling through covalent and noncovalent pathways in proteins. *J Chem Phys* 86:4488–4498.
33. Beratan DN, et al. (2015) Charge transfer in dynamical biosystems, or the treachery of (static) images. *Acc Chem Res* 48:474–481.
34. Breuer M, et al. (2012) Molecular structure and free energy landscape for electron transport in the deca-heme cytochrome mtrf. *Biochem Soc Trans* 40:1198–1203.
35. Blumberger J (2008) Free energies for biological electron transfer from qm/mm calculation: Method, application and critical assessment. *Phys Chem Phys* 10: 5651–5667.
36. White GF, et al. (2013) Rapid electron exchange between surface-exposed bacterial cytochromes and fe(iii) minerals. *Proc Nat Acad Sci USA* 110:6346–6351.
37. Xu S, Barrozo A, Tender LM, Krylov AI, El-Naggar MY (2018) Multiheme cytochrome mediated redox conduction through shewanella oneidensis mr1 cells. *J Am Chem Soc* 140:10085–10089.
38. Polizzi NF, Skourtis SS, Beratan DN (2012) Physical constraints on charge transport through bacterial nanowires. *Faraday Discuss* 155:43–62.
39. Pirbadian S, El-Naggar MY (2012) Multistep hopping and extracellular charge transfer in microbial redox chains. *Phys Chem Phys* 14:13802.
40. Rabaey K, Rozendal RA (2010) Microbial electrosynthesis - revisiting the electrical route for microbial production. *Nat Rev Microbiol* 8:706–716.
41. Barchinger SE, et al. (2016) Regulation of gene expression in shewanella oneidensis mr-1 during electron acceptor limitation and bacterial nanowire formation. *Appl Environ Microbiol* 82:5428–5443.
42. Edwards MJ, et al. (2015) Redox linked flavin sites in extracellular decaheme proteins involved in microbe-mineral electron transfer. *Sci Rep* 5:11677.
43. Duan Y, et al. (2003) A point-charge force field for molecular mechanics simulations of proteins based on condensed-phase quantum mechanical calculations. *J Comp Chem* 24:1999– 2012.
44. Jorgensen WL, Chandrasekhar J, Madura JD, Impey RW, Klein ML (1983) Comparison of simple potential functions for simulating liquid water. *J Chem Phys* 79: 926–935.
45. Kondov I, Cizek M, Benesch C, Wang H, Thoss M (2007) Quantum dynamics of photoinduced electron-transfer reactions in dye,àísemiconductor systems:,Äâ first-principles description and application to coumarin 343-tio2. *J Phys Chem C* 111:11970–11981.
46. Futera Z, Blumberger J (2017) Electronic couplings for charge transfer across molecule/metal and molecule/semiconductor interfaces: Performance of the projector operator-based diabatization approach. *J Phys Chem C* 121:19677–19689.
47. Kubas A, et al. (2014) Electronic couplings for molecular charge transfer: Benchmarking cdft, fodft and fodftb against high-level ab initio calculations. *J Chem Phys* 140:104105–104121.
48. Leys D, et al. (2002) Crystal structures at atomic resolution reveal the novel concept of ‚Äòelectron-harvesting‚Äô as a role for the small tetraheme cytochrome c. *J Biol Chem* 277:35703–35711.
49. Winn MD, et al. (2011) Overview of the ccp4 suite and current developments. *Acta Cryst Sec D* 67:235–242.